CZECH TECHNICAL UNIVERSITY IN PRAGUE

Faculty of Nuclear Sciences and Physical Engineering

Department of Physics

Research project

Analysis of D0 meson production in Cu+Au collisions in the STAR detector

Miroslav Šaur

Supervisor: Mgr. Pavol Federič Ph.D

Consultant: Mgr. Jaroslav Bielčík Ph.D

Prague, 2016

ČESKÉ VYSOKÉ UČENÍ TECHNICKÉ V PRAZE
FAKULTA JADERNÁ A FYZIKÁLNĚ INŽENÝRSKÁ
PRAHA 1 - STARÉ MĚSTO, BŘEHOVÁ 7 - PSČ 115 19

Katedra: fyziky **Akademický rok:** 2015/2016

VÝZKUMNÝ ÚKOL

Posluchač: Bc. Miroslav Šaur

Obor: Experimentální jaderná a částicová fyzika

Vedoucí úkolu: Mgr. Pavol Federič, Ph.D., Ústav jaderné fyziky, AV ČR, v.v.i.

Konzultant: Mgr. Jaroslav Bielčik, Ph.D., FJFI ČVUT

Název úkolu (česky/anglicky):
Analýza produkce mezonu D0 v Cu+Au srážkách v experimentu STAR
Analysis of D0 meson productionin in Cu+Au collisions in the STAR experiment

Pokyny pro vypracování:

1. Detailně se seznámit s experimentem STAR a s fyzikou srážek ultrarelativistických těžkých jader.

2. Studium produkce D0 mezonů v Cu+Au srážkách na experimentu STAR v hadronovém rozpadovém kanálu.

Součástí zadání výzkumného úkolu je jeho uložení na webové stránky katedry fyziky.

Literatura:

[1] Observation of D0 Meson Nuclear Modifications in Au+Au Collisions at √sNN=200 GeV, Phys. Rev. Lett. **113**, 142301
[2] Measurements of D0 and D* production in p+p collisions at s√NN=200 GeV, Phys. Rev. D **86**, 072013
[3] K. Yagi et al., Quark-gluon plasma, Cambridge University Press, (2005)

Datum zadání: 23.10.2015 .....

Datum odevzdání: 24.06.2016 ***Vedoucí katedry***

Prohlášení:

Prohlašuji, že jsem výzkumný úkol vypracoval samostatně a použil jsem pouze podklady (literaturu, software, atd.) uvedené v přiloženém seznamu.

Nemám závažný důvod proti užití tohoto školního díla ve smyslu 60 Zákona .121/2000 Sb., o právu autorském, o právech souvisejících s právem autorským a o změně některých zákonů (autorský zákon).

V Praze dne 23.6.2016

Title:
Analysis of D0 meson production in Cu+Au collisions in the STAR detector

Author: Miroslav Šaur

Specialization: Experimental nuclear and particle physics

Sort of project: Research project

Supervisor: Mgr. Pavol Federič, Ph.D.
Consultant: Mgr. Jaroslav Bielčík, Ph.D.
Abstract: In the ultra-relativistic heavy-ion collisions is created new state of matter : quark-gluon plasma (QGP). In this state of matter quarks and gluons behaves as free particles, which are confined at standard hadronic matter. QGP is studied at experiment STAR at Relativistic Heavy Ion Collider. Heavy quarks produced by hard processes before creation of QGP can serve as probes of QGP. In this work first results of analysis of D^0 meson production at Cu+Au collisions will be shown.

Key words: nucleus-nucleus collisions, quark-gluon plasma, hard processes, detector STAR, D^0 meson

Název práce:
Analýza produkce mezonu D0 v Cu+Au srážkách v eperimentu STAR

Autor: Miroslav Šaur

Supervisor: Mgr. Pavol Federič, Ph.D.
Consultant: Mgr. Jaroslav Bielčík, Ph.D.
Abstrakt: V ultrarelativistických jádro-jaderných srážkach je vytvářen nový stav hmoty: *kvark gluonove plazma*. V této fázi hmoty se kvarky a gluony chovají jako volné castice, což za normalních podmínek není možné. Kvark gluonové plazma muže byt studováno na experimentech STAR a PHENIX na Urychlovači relstivistických ťežkých iontů. Tězké kvarky produkované těsne po srážce mohou sloužit jako sonda QGP. V této praci budou prezentovány první výsledky analýzy produkce D^0 mezonu v Cu+Au srážkach.
Klíčová slova: jádro-jaderné srážky, kvark-gluonové plazma, tvrdé procesy, detektor STAR, D^0 meson.

Acknowledgement

I would like to thank my supervisor Mgr. Pavol Federič Ph.D. for his advices, support and great patience during working on this thesis. I would also like thank my consultant Mgr. Jaroslav Bielčík Ph.D. for his advices and for offering opportunity to work on this thesis.

Contents

List of Figures

List of Tables

Introduction

One of the main part of contemporary high-energy physics are ultra-relativistic heavy-ion collisions, in which hadronic matter is under extreme conditions. Experimental results favoured explanation that the matter undergoes phase shift from normal state to QGP which is strongly interacting. This we phase of matter can be studied by various method. One of method of study QGP is to study production of different types of particles in heavy-ion collisions and compare results with data from proton-proton collisions. Obtained difference tell us, how much QGP modified production of particles and how particles propagates through QGP.

This research project is divided at four main parts. The first chapter is about experimental setup, Relativistic Heavy Ion Collider, STAR detector and its sub-detectors which are used for this analysis are described. At the end of this chapter the future projects of sPHENIX detector and proposed modernization of Relativistic Heavy Ion Collider - eRHIC- are presented. The second chapter provides a brief theoretical overview about fundamental theories and processes. Standard model of Particle physics, strong interactions and its theoretical description are introduced. Then general informations about heavy-ion collisions, the timeline of collisions, quark-gluon plasma and D^0 meson are shown. Next chapter, the third, discuss chosen experimental results from various experiment (STAR, ALICE) and various collided systems (p+p, p+Pb, Au+Au, Pb+Pb) about production of D^0 mesons. In the fourth chapter first results of analysis of D^0 meson production in Cu+Au collisions in the STAR detector are shown.

Chapter 1

Experimental setup

In this chapter the experimental setup will be described. At first will be described RHIC, than STAR detector and sub-detectors of the STAR. After that description, current and planned physical runs of RHIC are mentioned. End of the chapter is dedicated to brief overview of two upgrades which affects RHIC: sPHENIX and eRHIC.

1.1 RHIC

Relativistic Heavy Ion Collider (RHIC) is located at Brookhaven National Laboratory (BNL) on Long Island, USA. RHIC is a synchrotron (storage ring) based accelerator, scheme of RHIC complex can be seen at Fig. 1.1. One of the main goal of RHIC is to study the quark-gluon plasma. The formal RHIC proposal was issued in August 1984, actual construction began at 1991. The construction of RHIC was completed in 1999, first physics run take place at June 12, 2000. Two Au beams was collided with energy per nucleon $\sqrt{s_{NN}} = 28\ GeV$ [2]. RHIC itself consist of independent rings - called "Yellow" and "Blue" - where in Blue ring the beam is in clock-wise direction and in Yellow ring beam is in counter clock-wise direction. Nominal energies of RHIC are $\sqrt{s_{NN}} = 200\ GeV$ for ions and $\sqrt{s} = 500\ GeV$ for protons.

Main physics goal of RHIC is to study formation of quark-gluon plasma (QGP), describe the transition between hadronic phase of mater and QGP and also RHIC have rich program studying spin of proton. To accomplish this goals, RHIC has collided polarized protons, deuterons and isotopes $^{27}_{13}$Al, $^{63}_{29}$Cu, $^{197}_{79}$Au, $^{238}_{92}$U. There were symmetrical collisions p+p, Cu+Cu, Au+Au, U+U and also several non-symmetrical geometries: p+Au,p+Al,d+Au, He+Au, Cu+Au. Even some fixed target experiments takes place at RHIC. Cu+Au collisions will be more described in chapter dedicated to theory. Summary of collisions energies, species combinations and luminosities can be seen at Fig. 1.2.

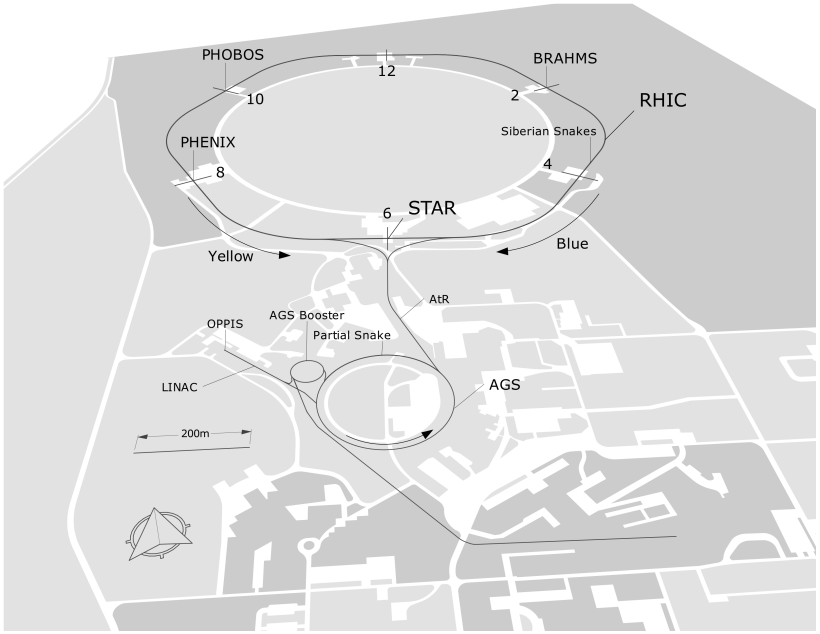

Figure 1.1: Layout of Relativistic Heavy Ion Collider and pre-accelerators [1].

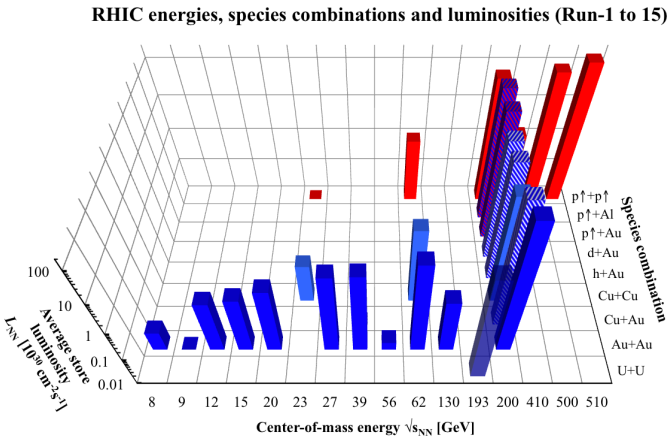

Figure 1.2: Summary of collisions energy, species combinations and average store luminosity from run 1 (2001) to run 15 (2015).[3]

Nowadays only two of original four detectors at RHIC are still active: STAR and PHENIX. Detectors PHOBOS and BRAHMS are already finish their physical program and are not longer active. Detectors STAR and

PHENIX both study QGP, where PHENIX is mainly dedicated tu study QGP via prompt electrons and photons.

1.2 STAR detector

The Solenoidal Tracker At RHIC (STAR) detector main purpose is tu study hot and dense nuclear matter in heavy-ion collisions via detecting, tracking and identifying charged particles in mid-rapidity. STAR detector consist of room-temperature solenoid magnet with full field strength $B = 0.5T$ which surrounds most of detector subsystems. Magnetic field is parallel to beam axis. STAR detector[1] is a combination of 13 sub-detectors, where 6 sub-detectors are azimuthally symmetrical (from inner to outer):

- Heavy flavour tracker (HFT), which consist of:
  - PiXel detector (PXL)
  - Intermediate Silicon Tracker (IST)
  - Silicon Strip Tracker (SST)
- Time of Flight (TOF)
- Time Projection Chamber (TPC)
- Barrel ElectroMagnetic Calorimeter (BEMC)
- Muon Telescope Detector (MTD)
- Forward Time Projection Chamber (TPC)

There are two categories of non-symmetrical sub-detectors. First category are 2 detectors in the forward rapidity region ($1.086<\eta<2$):

- Endcap Electromagnetic Calorimeter (EEMC)
- Forward GEM Tracker (FGT)

Second category are 3 fast triggering detectors:

- Vertex Position Detector (VPD)
- Beam-beam counter (BBC)
- Zero degree Calorimeter (ZDC)

Schematic view of STAR detector can be seen at 1.3.

For purpose of this work following sub-detectors will be more thoroughly described: Time Projection Chamber, Time of Flight detector and Vertex Position Detector as they are crucial for data analysis.

[1] As in 2015.

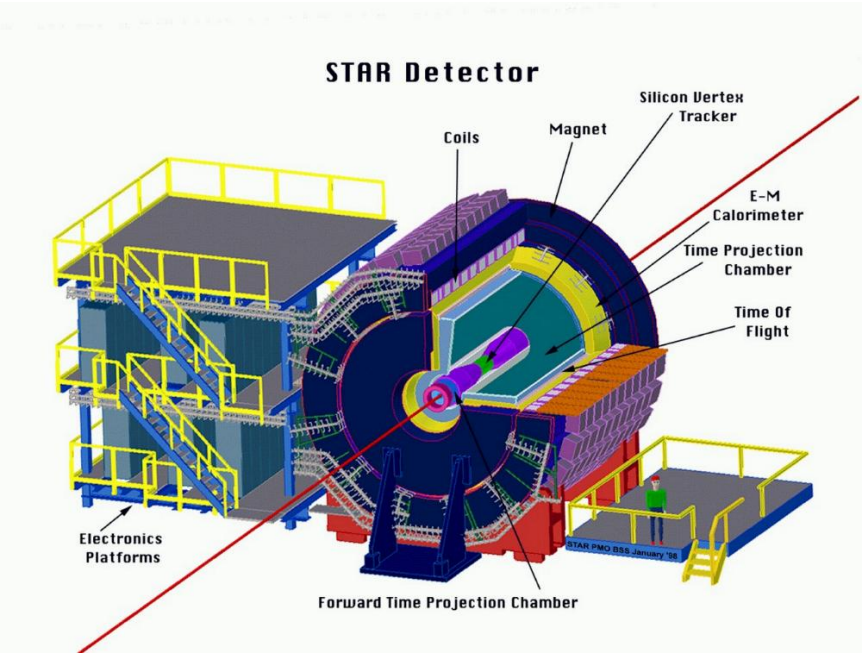

Figure 1.3: Schematic view of STAR detector at RHIC. Taken from [**?**]

1.2.1 Time Projection Chamber

Time Projection Chamber (TPC) is primary tracking sub-detector of charged particles. Also TPC identifying particles via their specific ionization energy loss.

The TPC is cylindrical tracking device with full azimuthal angle ($0<\phi<2\pi$). TPC is cylinder with outer diameter $r_{out} = 4m$ and inner $r_{in} = 1m$, with length 4.2 m (Fig. 1.4). Pseudorapidity coverage is ± 1.8 units.

Internally TPC is divided into two halves (at $z = 0$) along the beam pipe by the High Voltage Membrane. Voltage of membrane is $-28kV$ and serve as TPC cathode. Internally TPC divided by a equipotential rings which forms the field cage. Multi-wire proportional chambers (MWPC) serves as anode, and with membrane and field cage creating together uniform electric field of $E \sim 135V/cm$. Cylinder volume is filled with P10 gas (10% of methane and 90% of argon) with pressure 200 Pa above atmospheric pressure.

The MWPC are divided into 12 sector, in each sector there are 13 inner and 32 outer pad rows. In total MWPC consist of 136 560 read-outs pads. Fig 1.5 shows geometry of one section of MWPC.

Charged particle traversing the volume of TPC ionizing P10 gas. Electrons then drifts towards anode at a average velocity $v_{e,drift} = 5.45cm/\mu s$, resulting in maximum drift time in the TPC $t_{max,drift} = 40\mu s$. Drift velocity depends on temperature and pressure inside TPC.

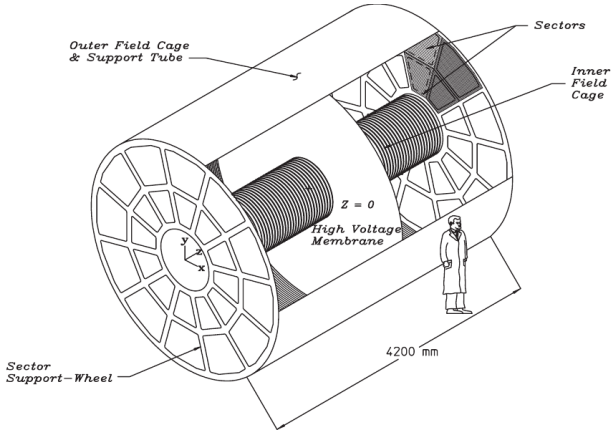

Figure 1.4: Schematic view of Time Projection Chamber sub-detector of STAR [4].

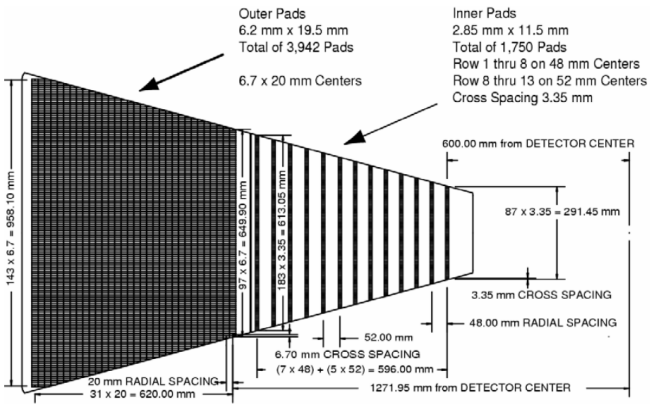

Figure 1.5: Schematic view of the anode pad plane [4].

1.2.2 Time of Flight detector

Time-of-Flight detector (TOF) is designated to measure time of flight of particle and together with TPC to obtain information about masses and velocity of particles passing through TPC and TOF. TOF consist of Barrel TOF (BTOF) and the Vertex position Detector (VPD).

BTOF consist of 120 trays that cover full azimuthal angle and pseudo-rapidity at ± 1.8 units. Sub-detector itself is based on Multi-gap Resistive Plate Chamber (MRPC) technology, which using collection of currents induced by alternation of electric field that is caused by electron avalanches created in detector gas. Each tray of BTOF has 32 MRPC modules, each module containing 6 pads. Geometry of BTOF is shown at Fig. 1.6.

The VPD is a coincidental detector and consist of two identical parts

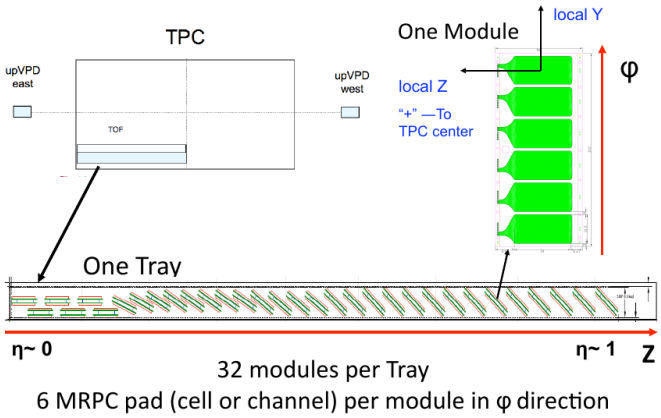

Figure 1.6: Geometry of Barrel Time of Flight detector. Figure taken from [9]

on the west and east side of the beam pipe, 5.7 m from centre of STAR detector. Each part consist of 19 cylindrically shaped channels of lead layers, scintillator and a photo-multiplier tube. The VPD measures the star time and BTOF measure stop time. Then we have

$$stop\ time - start\ time \equiv \tau$$

where τ is proper time of particle.

1.3 Current and planned runs

Run-15 consisted of 22.4 cryo-weeks and takes place from 24.01.2015 to 28.07.2015. During Run-15 3 types of collisions takes place: p+p, p+$^{197}_{79}$Au and p+$^{27}_{13}$Al. Run-15 is summarized at 1.1.

System	E [GeV/nucleon]	T	L
polarized p+p	100.2	10.9 weeks	382 pb^{-1}
polarized p + $^{197}_{79}$Au	103.4 + 97.4	5.1 weeks	1.27 nb^{-1}
polarized p + $^{27}_{13}$Al	103.4 + 98.6	1.9 weeks	3.97 pb^{-1}

Table 1.1: Overview of Run-15. E is a total energy per nucleon, T is duration of each type of collisions, L is a total delivered luminosity.

For the year 2016 there are planned 20 cryo-weeks. Run-16 started at 25.01.2016 and end of the Run-16 is planned for June 2016. Specific informations about Run-16 are in Tab. 1.2.

System	E [GeV/nucleon]	T	L
$^{197}_{79}$Au + $^{197}_{79}$Au	100.0	13.1 weeks	46.1 nb^{-1}
d + $^{197}_{79}$Au	100.0 + 100.7	8 days	289 nb^{-1}
d + $^{197}_{79}$Au	31.2	6 days	44 nb^{-1}
d + $^{197}_{79}$Au	9.8	in progress	-
d + $^{197}_{79}$Au	19.5	in preparation	-

Table 1.2: Overview of Run-16. E is a total energy per nucleon, T is duration of each type of collisions, L is a total delivered luminosity.

For next years (2017, 2018), there are still discussions about scheme of particular runs, but two main scenarios are[2]:

- Version 1: 19 cryo-weeks in the Run-17, 13 cryo-weeks in the Run-18 (table 1.3)
- Version 2: 24 cryo-weeks in the Run-17, 13 cryo-weeks in the Run-18 (table 1.4)

Run	System	E [GeV/nucleon]	Duration [week]
17	Transverse p+p	500	13
17	p+p	500	1
17	CeC	500	2
18	$^{96}_{44}$Ru+$^{96}_{44}$Ru	200	3.5
18	$^{96}_{40}$Zr+$^{96}_{40}$Zr	200	3.5
18	$^{197}_{79}$Au+$^{197}_{79}$Au	27	2

Table 1.3: Overview of version 1 of Run-17 and 18. 19 cryo-weeks for Run-17 and 13 cryo-weeks for Run-18. E is a total energy per nucleon. CeC is Coherent electron Cooling.

Collisions of isobaric nuclei $^{96}_{44}$Ru and $^{96}_{40}$Zr provides a opportunity to study chiral magnetic and vortical effects. Energy of collisions is planned as $\sqrt{s_{NN}} = 200\ GeV$ and is predicted to take 1.2 milliard events. Chiral effects are long discussed and experimental results so far supports chiral magnetic effects, chiral magnetic wave and chiral vortical effects. Ratio of multiplicity () of Ru and Zr is almost identical (excluding 0-5% most central collisions) but they had different nucleus deformity β_2. For Ru $\beta_2 = 0.158$, for Zr $\beta_2 = 0.08$ - these are results from e-A scattering[3].

[2]According the Beam Use Request from May 26, 2016

[3]According different sources - comprehensive model deductions - deformity parameter is $\beta_2 = 0.053$ for Ru and $\beta_2 = 0.217$ for Zr, which is quiet opposite to results from e-A scattering.

Run	System	E [GeV/nucleon]	Duration [week]
17	Transverse p+p	500	13
17	p+p	500	1
17	CeC	500	2
18	$^{197}_{79}$Au+$^{197}_{79}$Au	62.4	4
18	$^{96}_{44}$Ru+$^{96}_{44}$Ru	200	3.5
18	$^{96}_{40}$Zr+$^{96}_{40}$Zr	200	3.5
18	$^{197}_{79}$Au+$^{197}_{79}$Au	27	2

Table 1.4: Overview of version 2 of Run-17 and 18. 24 cryo-weeks for Run-17 and 13 cryo-weeks for Run-18. E is a total energy per nucleon. CeC is Coherent electron Cooling.

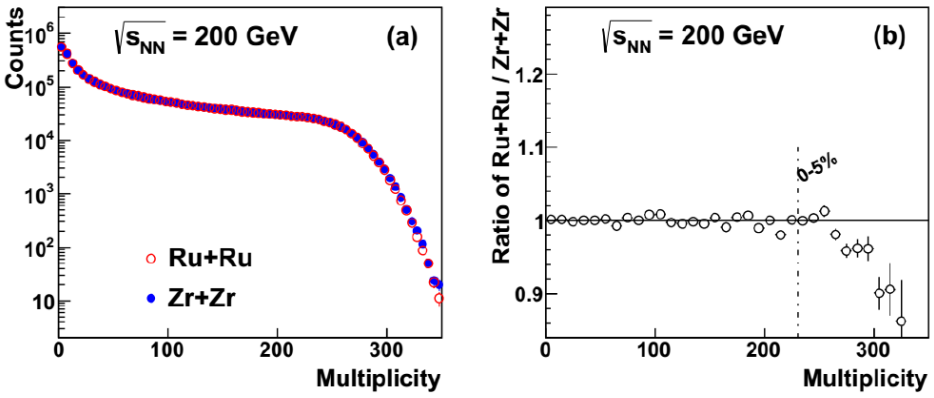

Figure 1.7: Panel (a): The Glauber model multiplicity simulation for Ru and Zr. Panel (b): Ratio of the Glauber model multiplicity. The solid lines represents calculations with Glauber model, dashed lines represent calculation with comprehensive model deductions. Taken from [28].

Due to different deformation the initial magnetic field would be different for Ru+Ru and Zr+Zr collisions. Theoretical calculations for initial distribution of magnetic field are show at 1.8. If there really are chiral and vortical effect, then those effects should be functions of $(\frac{eB}{m_\pi})^2 cos[2(\psi_B - \psi_{RP})]$, where e is elemental charge, B is magnetic field, m_π is mass of pion, ψ_B and ψ_{RP} are .

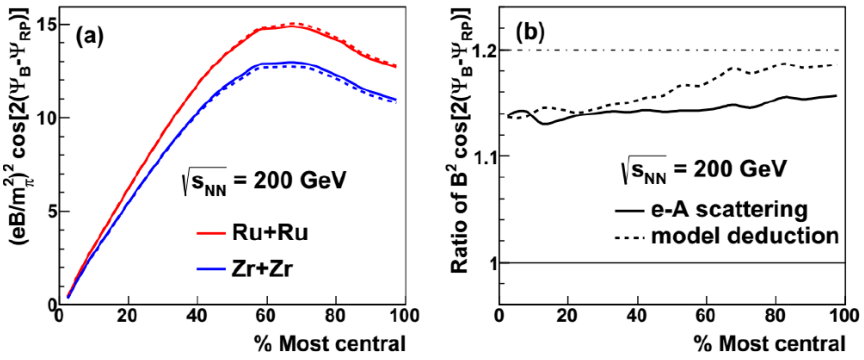

Figure 1.8: Panel (a):Initial magnetic field for Ru+Ru and Zr+Zr collisions. Panel (b): Ratio of distribution versus centrality. The solid lines represents calculations with Glauber model, dashed lines represent calculation with comprehensive model deductions. Taken from [28].

1.4 Future of RHIC

1.4.1 sPHENIX

One of the major upgrades of RHIC since it's operational start is project sPHENIX. PHENIX collaboration proposed at 2012 a major upgrade of PHENIX detector which should open new possibilities for studying of QGP. Technically sPHENIX is completely new detector. This upgrade was approved at 2015.

sPHENIX collaboration proposed measurement mainly of following systems:

- jets
- b-tagged jets
- photons
- charge hadrons and their correlations
- measurement of Υ particles family

Cross section of proposed new detector is shown at Fig. 1.9. The sPHENIX detector should consist of (fron inner to outer layer):

- Silicon tracker
- Electromagnetic calorimeter - EMCal
- Inner hadronic calorimeter - IHCal

- Solenoid magnet
- Outer hadronic calorimeter - Outer HCal

Silicon tracker is designed as seven layer silicon detectors. Goal of silicon tracker is reconstruction of charged tracks and determination of particle momentum.

Electromagnetic calorimeter is a tungsten-scintillating fibre sampling calorimeter with silicon photo-multipliers read-out system.

Hadronic calorimeter, a sampling calorimeter, is divided into two pieces - outer (HCal) and inner (IHCal) hadronic calorimeter. IHCal consist of non-magnetic metal and scintillator located inside the bore of solenoid magnet. Outer HCal consist of steel scintillator which is outside of the cryostat.

Silicon tracker is designed as seven layer silicon detectors. Goal of silicion tracker is reconstruction of charged tracks and determination of particle momentum.

Magnet of sPHENIX will be taken from BaBar experiment. Is is a solenoid magnet with operating current $I_{op} = 4596\text{A}$ and maximal intensity of magnetic field $B = 1.5\text{T}$. Property of magnet is already transferred from SLAC to BNL.

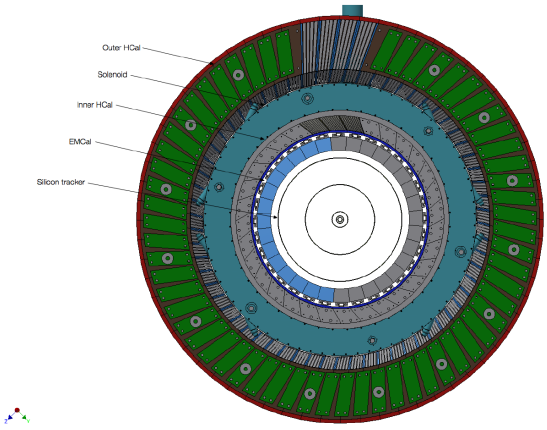

Figure 1.9: Cross section of sPHENIX detector. Taken from [5]

sPHENIX collaboration expect that sPHENIX detector should be fully operational at the star of 2021 run. More about sPHENIX can be found at [5].

1.4.2 eRHIC

Proposed *Electron Ion Collider* (EIC) is a great step at experimental possibilities in high energy physics. Proposed idea of colliding electrons with heavy ions opens many new areas of research which are not possible reached

with current experimental technologies. For a few lets name a gluon saturation, test of QCD at extreme conditions, precise measurements of spin distribution inside a proton and more. Realization of EIC at RHIC should bear name eRHIC. More about eRHIC can be found at [6].

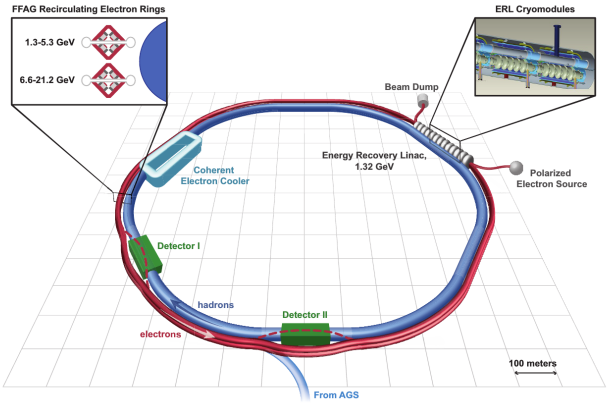

Figure 1.10: The layout of eRHIC collider. Taken from [6].

Chapter 2

Theory overview

RHIC discovered new phase of matter called *quark-gluon plasma* (QGP) in Au+AU collisions at 2004 [11]. The QGP is produced in heavy-ion collisions with high energy densities, where temperature of system cross the critical temperature $T_c = 170MeV$. One possible way to study QGP is to study modification of various particle production in heavy-ion collisions (where is believed that QGP is created) compared to proton-proton collisions. In this chapter a brief theoretical overview about hard processes, heavy-ion collisions, quark-gluon plasma, D^0 meson will be discussed.

2.1 The Standard model of particle physics

The Standard model of particle physics is a theory describing 3 of 4 known interactions (strong, weak, electromagnetic, gravitational), 5 gauge bosons $gluon, W^{+/-}, Z^0, \gamma$, (spin $= \hbar$) which intermediate fundamental interactions, 12 elementary fermions (spin $= \hbar/2$). Fermions are more divided at 6 leptons: *electron* (e), *muon* (μ), *tau* (τ), *electron neutrino* (ν_e), *muon neutrino* (ν_μ), *tau neutrino* (ν_τ), and 6 quarks: *up* (u), *down* (d), *charm* (c), *strange* (s), *top* (t), *bottom* (b). Each fermion also have its own antiparticle. Table of particles of Standard model are shown at 2.1. Mathematically the Standard model is a non-abelian gauge theory with the symmetry group $SU(3) \times SU(2) \times U(1)$.

Fundamental interactions included at Standard model are:

- Strong nuclear interaction - described by quantum chromodynamics
- Weak nuclear interaction - described by electro-weak theory
- Electromagnetic interaction - described by quantum electrodynamics

Weak nuclear interaction and electromagnetic interaction are united in electroweak interaction.

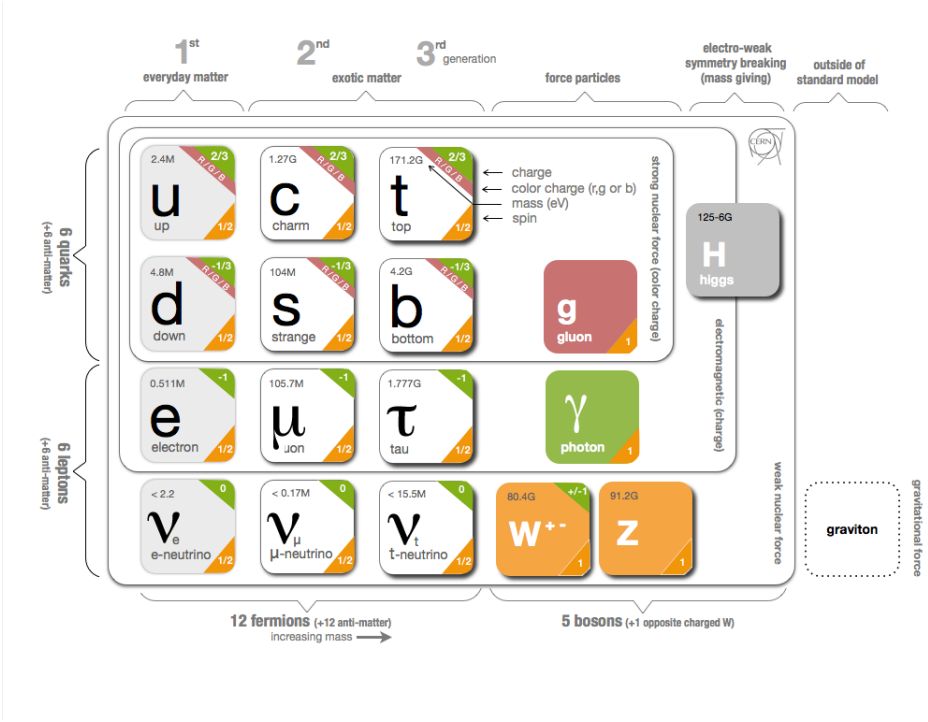

Figure 2.1: Particles of Standard model and their interactions. Taken from [30].

According the Standard model quarks forms the *mesons* - a bounded state of quark and anti-quark, and *baryons* - bounded state of three quarks. Mesons and baryons are collectively called as a *hadrons*. In the past few years there are a few results about *tetraquark* [17]- a bounded state of four quarks, and *pentraquark* - a bounded state of five quarks [29].

2.2 Strong interaction

Strong interaction is described by quantum chromodynamics (QCD). It is a non-abelian field theory with $SU(3)$ group of symmetry. QCD defines a new quantum number - *colour charge* or *colour*. There are 3 basic colours: *red* (r), *green* (g), *blue* (b). To any of these colours anti-colour exist. Gluons carry combination of colour and anti-colour charge, which create 9 combinations, but only 8 combinations intermediate strong interaction (last combination is white or colourless):

$$r\bar{g}, r\bar{b}, b\bar{g}, g\bar{r}, g\bar{b}, b\bar{b}, \frac{1}{\sqrt{2}}(r\bar{r} - g\bar{g}), \frac{1}{\sqrt{6}}(r\bar{r} + g\bar{g} - 2b\bar{b})$$

All observed particles are colourless. These combinations are called *hadrons*. Two main distinctive features of strong interactions are *asymptotic freedom*

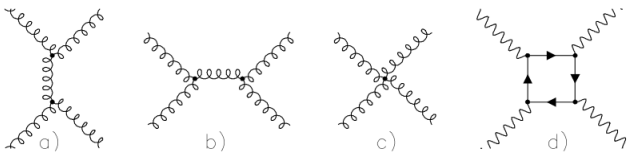

Figure 2.2: Schematic view of gluons interactions in Feynmann diagrams. [18]

and *confinement*. Another great difference of QCD against other interactions, for example QED, is that the gluons can interact between themselves as shown at Fig. 2.2.

The Lagrangian of QCD is given by

$$\mathcal{L} = \sum_q \bar{\psi_{q,a}}(i\gamma^\mu \partial_\mu \delta_{ab} - g_s \gamma^\mu t^C_{ab} \mathcal{A}^C_\mu - m_q \delta_{ab})\psi_{q,b} - \frac{1}{4} F^A_{\mu\nu} F^{\mu\nu A} \tag{2.1}$$

where over repeated indices are summed. The $\psi_{q,a}$ are quark-field spinors of quark with mass m_q and colour charge a that goes from 1 to 3 (one index for one colour charge). The γ^μ are Dirac gamma-matrices. The $\mathcal{A}^C_\mu$ are gluons fields, where C goes from 1 to 8, as there are 8 types of gluons. The t^C_{ab} are 3×3 matrices represents generators of $SU(3)$ symmetry group. The $F^A_{\mu\nu}$ is field-strength tensors which describes interactions between gluons and is defined as:

$$F^A_{\mu\nu} = \partial_\mu \mathcal{A}^A_\mu - \partial_\nu \mathcal{A}^A_\mu - g_s f_{ABC} \mathcal{A}^B_\mu \mathcal{A}^C_\nu \tag{2.2}$$

where

$$[t^A, b^B] = i f_{ABC} t^C$$

and f_{ABC} are structure constants of SU(3) group.

The fundamental parameters of QCD are coupling constant of strong interaction g_s (coupling constant can be equally written as: $\alpha_s = \frac{g_s^2}{4\pi}$) and masses of each quark m_{q_i}.

2.2.1 Asymptotic freedom

Asymptotic freedom can be explained via so-called Cornell potential[1] and as is present at 2.3 is valid only for static case and without temperature dependence.

$$V(r) = -\frac{4}{3}\frac{\alpha_s}{r} + \sigma r \tag{2.3}$$

[1]This potential is used as general QCD potential, but was primarily derived for quarkonium(*quarkonium* - a bounded state of heavy quark a its own anti-quark. *Charmonium* $-$ $c\bar{c}$, *bottomium* $-$ $b\bar{b}$)

where α_s is a alternative expression for coupling constant of strong interaction r is a distance, σ is a *string tensionconstant* which represents tension of colour field between valence quarks in meson in string model. As can be seen from 2.3 for small distances Coulomb term $\frac{\alpha_s}{r}$ dominates and potential is repulsive for quark-antiquark pair. However for large distances linear part of potential, σr, linearly rising and is responsible for colour confinement.

The effective QCD coupling constant α_s in the terms of renormalization theory can be expressed as

$$\alpha_s \approx \frac{4\pi}{\beta_0 ln(\mu^2/\Lambda^2_{QCD})} \approx \frac{12\pi}{25 ln(Q^2/\Lambda^2)} \tag{2.4}$$

where β_0 is a , μ^2 is a renormalization scale, Λ^2_{QCD} is scale of QCD. In second expression Λ^2 is cutoff parameter unique for each value of Q^2. As can be seen from Fig. 2.4 for fixed $\beta_0 > 0$, the α_s have only μ^2 functional dependence, so with increasing μ^2 effective constant α_s decreases. This implies that for short distances or for high transferred momentum coupling constant goes to 0 and quarks behaves as a free particles.

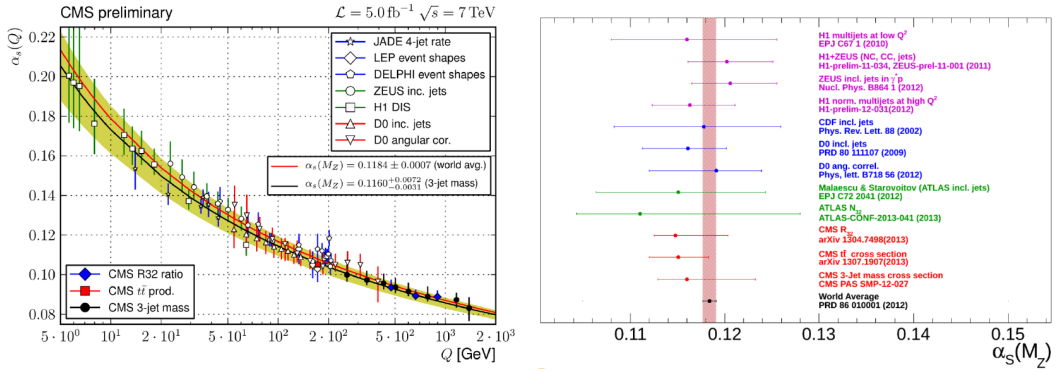

(a) Running α_S dependence on transferred momentum.

(b) Measurements of $\alpha_S\,(M_Z)$.

Figure 2.3: Measurements of strong coupling constant α_s. [10]

2.2.2 Colour confinement

As had been already said earlier, all observed particles are without colour charge, or can be said with *white* colour charge. From behaviour of Cornell potential 2.3 at larger distances coupling between quark and anti-quark gets stronger to the point when enough energy is stored in colour field (which is often depicted as a string) and new pair of quark and anti-quark is created. Colour field is often depicted as string which is Schematics of this process is shown at Fig. 2.4.

This model can explained why any particle with bare colour charge have not been observed, but this model in not a analytical proof within QCD.

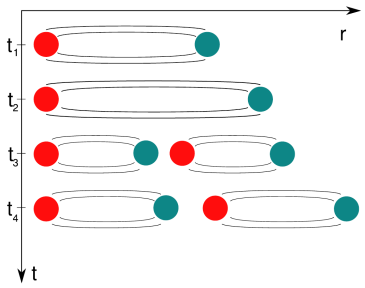

Figure 2.4: Schema of string breaking mechanism and creation of quark-antiquark pair. [10]

2.3 Hard processes

Generally all processes at particles or heavy-ions collisions can be divided at two main groups:

- Hard processes
- Soft processes

There is no clearly defined and generally acknowledged distinction between those two groups, but

Hard processes can be defined as processes with transferred momentum Q^2 greater than hundreds of GeV , and/or processes that can be described by *perturbative QCD* (pQCD) [7] [14].

Hard probes can be defined as objects created by hard processes. According definition of hard processes above hard probes can be listed as:

- Hard jets and partons with high p_T
- Heavy quarks and hadrons with open flavour
- Heavy quarkoniums (J/ψ, Υ) and theirs excited states
- Direct photons
- Production of $W^{+/-}$ *a* Z^0 bosons

All of this probes are created very early after collisions and thus there is no modification from the QGP. Therefore hard probes cn serve as probe of the hot and dense medium.

2.3.1 Factorization theorem QCD

Main idea of factorization theorem is to divided the formulas to part which can be described (and enumerated) by non-pertubative QCD a to part which must be computed via pertubative QCD. This idea come from assumption, that any parton-parton interaction occurs much quicker that any long-distance interactions (but still within QCD space-time scale) that happens before or after the collision itself. If this assumption is true, than nucleus can be treated as system of free partons.

One of the main goals of QCD is computation of cross section of high p_T partons collision. For high energy partons collision the production of new parton with high momentum can be computed by *QCD factorization theorem.*

$$d\sigma^{hard}_{AB\to h} = f_{a/A}(x_1, Q^2) \otimes f_{b/B}(x_2, Q^2) \otimes d\sigma^{hard}_{ab\to c}(x_1, x_2, Q^2) \otimes D_{c\to h}(z, Q^2) \tag{2.5}$$

where:

- $$d\sigma^{hard}_{ab\to c}(x_1, x_2, Q^2)$$
  is the perturbative cross-section enumerated to the order of renormalization constant α_s
- $$f_{a/A}(x_1, Q^2)$$
  is a parton distibution function (PDF) - probability of finding quark a with momentum fraction $x = \frac{p_{parton}}{p_{nucleus}}$ in nucleus A. Non-perturbative part.
- $$D_{c\to h}(z, Q^2)$$
  is a fragmentation function (FF) describing the probability of fragmentation outgoing parton c into the observed hadron h with momentum $z = \frac{p_{hadron}}{p_{nucleus}}$. Non-perturbative part.

In the case of nucleus-nucleus collision, from 2.5 is implied, that total hard inclusive cross section scale as

$$d\sigma^{hard}_{AB} = A \cdot B \cdot d\sigma^{hard}_{pp} \tag{2.6}$$

where A and B is number of nucleons in each of colliding ions. $d\sigma^{hard}_{pp}$ is total hard inclusive cross for $p + p$ collision.

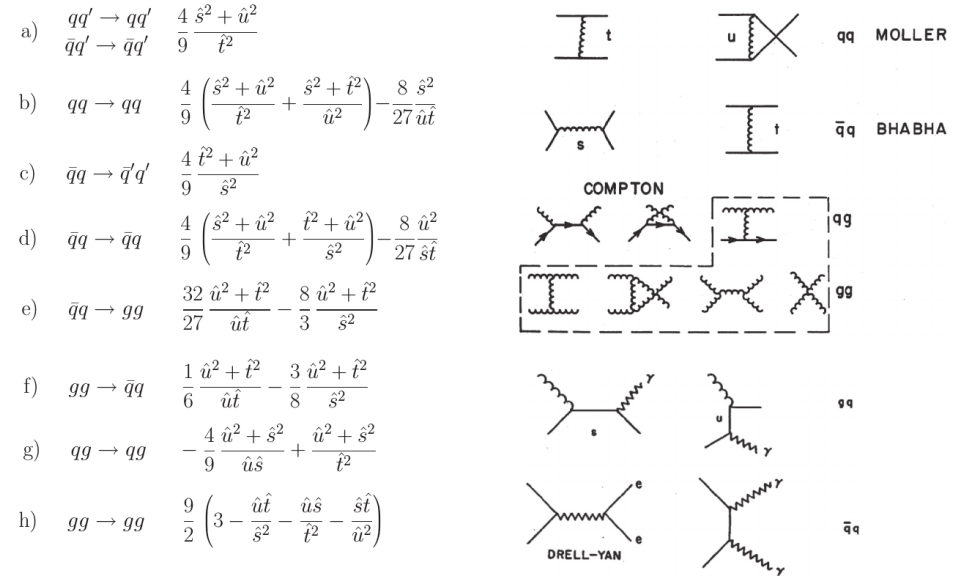

Figure 2.5: Hard scattering sub-processes in QCD. On the left side: (a)-(h) show different sub-processes for quarks q, antiquarks $\bar{q}$ and gluons g. On the right side: figures of the lowest order diagrams involving initial state q and g scattering. [14]

At 2.5 can be seen numerous sub-processes of QCD. First three subprocesses are analogues of processes from QED, respectively Moller, Bhabha and Compton scattering. Test of validity of these processes in QCD was one of the first proofs of validity of QCD.

2.4 Heavy-ion collisions

The goal of heavy-ion collisions is to produce and study a *hot and dense matter* which is expected to be a QGP.

Evolution of heavy-ion can be divided at 7 phases[2] - 1 pre-collision phase and 6 phases after collision:

1. Incoming hadrons - described by pQCD, saturation models and by *colour glass condensate* approach.

2. Hard scattering - described by pQCD. Highest energy density, creation of heavy quarks and hard probes. $\tau_{HS} \sim 0.1\ fm$

3. Glasma/strong fields - described by classical field theory.

[2]This division depends on author, in all of this work division according [7] is used.

4. Gluons and quarks out of equilibrium - described by kinetic theory.
5. Gluons and quarks at equilibrium - described by hydrodynamics.
6. Freeze out. Numbers and types of hadrons doesn't change any more.

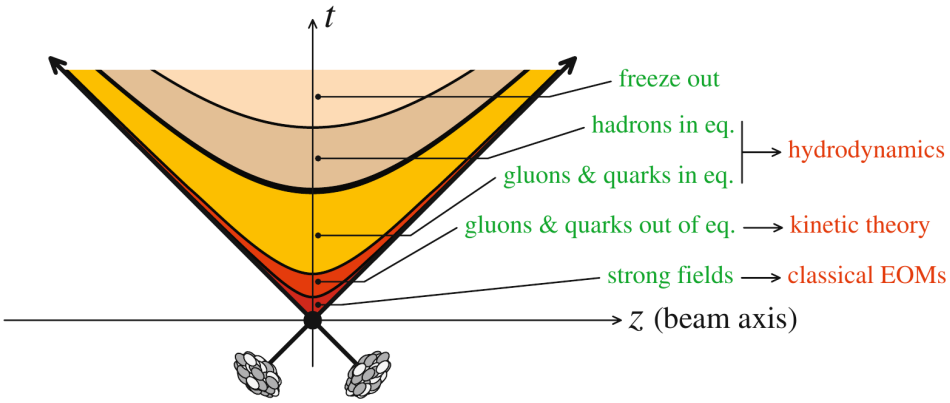

Figure 2.6: Timeline of heavy-ion collision with highlighted phases of collisions. [7]

Today, primarily two isotopes of heavy-ion are collided: $^{197}_{79}$Au at RHIC with $\sqrt{s_{NN}} = 200\ GeV$ and $^{208}_{82}$Pb at LHC with $\sqrt{s_{NN}} = 5.02\ TeV$.

2.4.1 Cu+Au collisions

In the year 2012 for 5.5 weeks, Cu+Au collisions take place at RHIC. Isotopes $^{63}_{29}$Cu and $^{197}_{79}$Au was collided with energy $\sqrt{s_{NN}} = 200GeV$. Primary motivation of Cu+AU collisions was a measurement of this system as a control geometry for Au+Au collisions, because according the Glauber model, number of participants in Cu+Au central collisions should agree with semi-central Au+Au collisions. Cu+Au system is asymmetrical both in longitude and transverse direction. Sketch of this system can be seen at 2.7

Another possibilities at Cu+Au collisions are studies of flow effect created by initial asymmetric density profile which lead to asymmetric pressure gradient and chiral effects due to sizeable initial electric field, which pointing from Au to Cu. This may lead to a charge dependence of directed flow.

2.5 Quark-gluon plasma

As already been said above, RHIC publish compelling evidence about existence of new hot and dense state of matter called quark-gluon plasma. Two main characteristics of QGP is *deconfinement* and restoration of *chiral symmetry*.

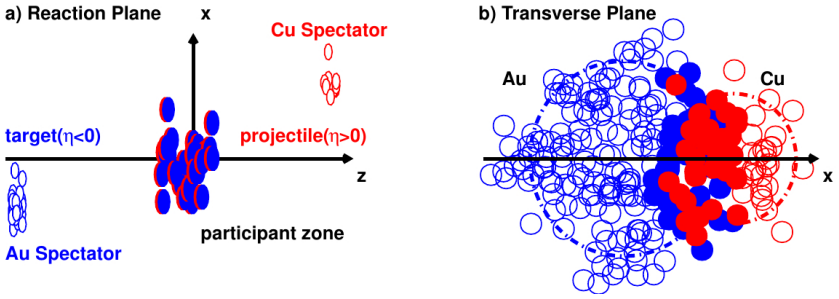

Figure 2.7: Schematic imagination of Cu+Au collision. a: View from a reaction plane. b: View from transverse plane. Taken from [19].

Quarks and gluons cannot be observed as free particles n normal conditions. But in the case of high temperature or high densities matter goes through phase transition and quarks and gluons becomes free. This is called as *deconfinement*, which is in accordance with QCD. For high temperatures Cornell potentoal 2.3 must be rewritten as:

$$V(r) = -\frac{4}{3}\frac{\alpha_s}{r}\exp^{-\mu_d r} + \sigma\frac{1-\exp^{-\mu_d r}}{\mu_d} \tag{2.7}$$

where $\mu_d = \mu_d(T) = \dfrac{1}{r_D}$ is Debye screening mass. For $r \ll \dfrac{1}{\mu_d}$ matter is in normal conditions and quarks and gluons are confinement in hadronic matter. But for $r \gg \dfrac{1}{\mu_d}$ deconfinement occurs, quarks and gluons are free.

Critical temperature is about $T_c = 170MeV$. One of the main goals of current heavy-ion physics is to find exact critical temperature T_c and nature of phase transition.

2.6 D^0 meson

D^0 meson is a bounded state of u quark and $\bar{c}$ quark (for $\bar{D^0}$ quark composition is $c\bar{u}$), with mass $m_{D^0} = (1864.84 \pm 0.007)$ GeV/c^2 [16]. First discovered at SLAC in 1976, D^0 is a lightest meson containing *charm* quark. For this feature D^0 is often used as one of the first probes of the medium.

Charm quarks are created at initial hard scattering with the minimum value of $Q^2 = 2m_c$, therefore space-time scale $\tau_c \sim 0.1\ fm$. Production of D^0 in heavy-ion collisions an be studied via semileptonic decay or by hadronic decay. Study of D^0 meson production via semileptonic decay i only indirect so this channel cannot give access to parent hadron kinematics and is more influenced by decay of hadrons with bottom quark. But semileptonic channel is easily trigerred and have higher branching ration. Hadronic decay give us direct access to parent hadron kinematics, but have smaller branching

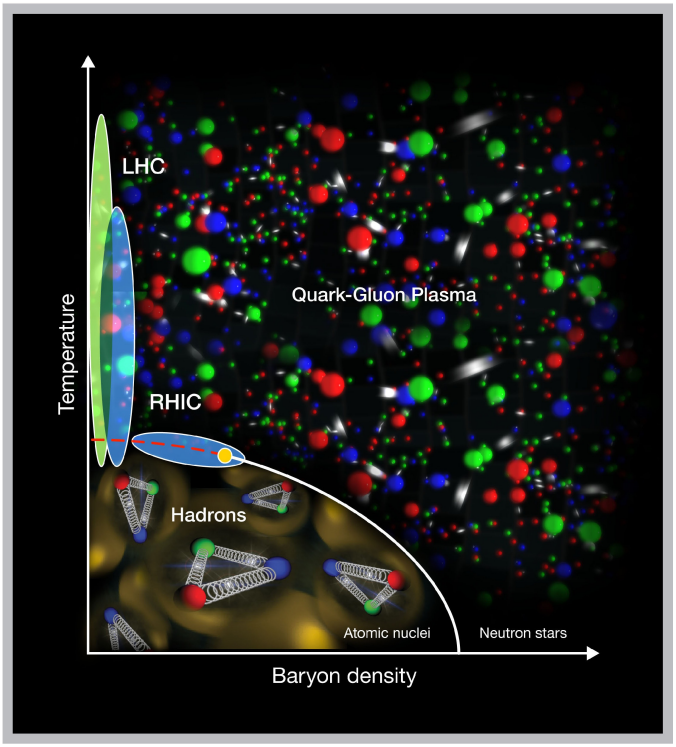

Figure 2.8: Phase diagram of matter with temperature and baryon density dependance. Areas that can be studied by RHIC and LHC are shown. Taken from [15].

ratio and larger combinatorial background. Schematic view of both decay channels is shown at Fig. 2.9.

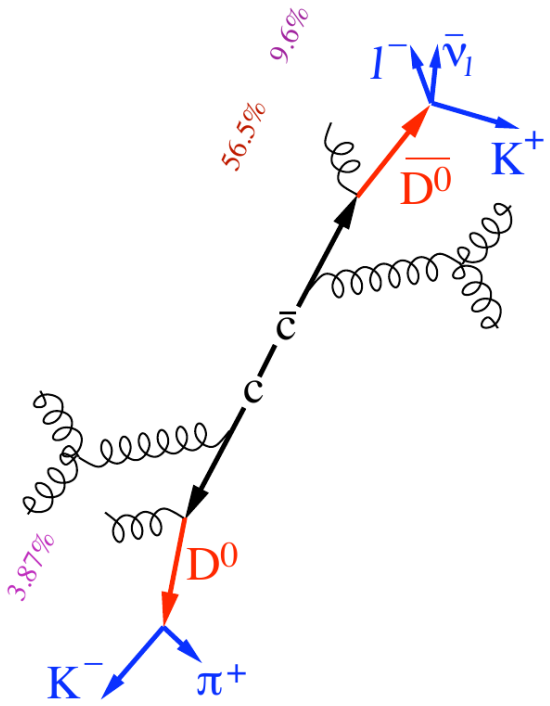

Figure 2.9: Fragmentation of c quark to D^0 meson and two main D^0 meson decay channels. [9]

Chapter 3

Overview of experimental results

In this chapter a brief overview of experimental results from measuring of D^0 meson in various systems will be discussed. Results are from experiment STAR at RHIC and from experiment ALICE at LHC. Moreover published results about modification of production of $J\psi$ from Cu+Au collisions at PHENIX detector at RHIC will be discussed.

3.1 Results from STAR

Production of D^0 meson at STAR was measured in numerous systems, for this overview were chosen results from p+p collisions at $\sqrt{s} = 200\ GeV$ and Au+Au collisions at $\sqrt{s_{NN}} = 200\ GeV$. Main sources for this section are: [9], [20], [22] and

3.1.1 p+p results

The data sample consisted of minimum-bias p+p collisions at $\sqrt{s} = 200\ GeV$ from 2009. D^0 and $D*$ were reconstructed via hadronic decay channel in the transverse momentum ranges 0.6-2.0 GeV/c and 2.0-6.0 GeV/c. Obtained invariant yield of D^0 is shown at 3.1.

Differential cross section for D^0 and $D*$ were extracted as is shown at 3.2. The D^0 and $D*$ cross sections were divided by the charm quark fragmentation ratios 0.565 ± 0.032 ($c \rightarrow D^0$) and 0.224 ± 0.028 ($c \rightarrow D^{?+}$). Result were compared to the theoretical models - FONLL (Fixed-Order-Next-to-Next-Leading Logarithm) pQCD and PYTHIA calculations. Result are consistent with upper limits of FONLL pQCD calculations. For comparing with PYTHIA, PYTHIA 6.416 with various tunes were used[1]. Total

[1]Full discussion of tunes and results are in [20].

charm cross section at $\sqrt{s} = 200\ GeV$ was estimated as:

$$\sigma_{c\bar{c}} = 797 \pm 210(stat.)^{+208}_{-295}(sys)\ \mu b$$

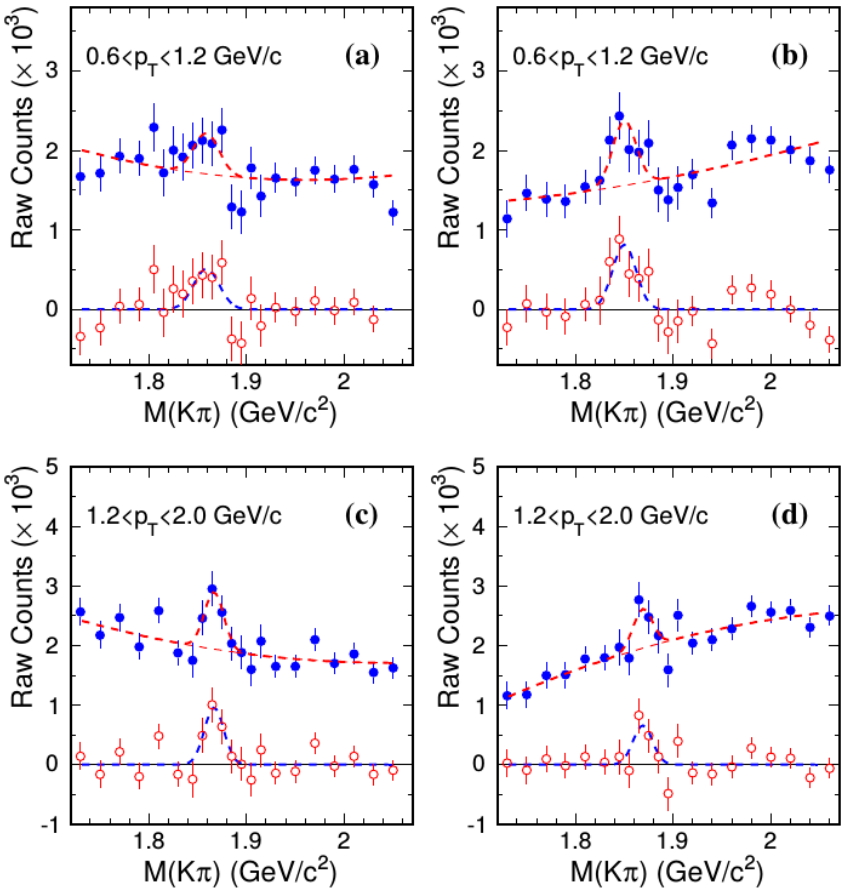

Figure 3.1: Raw D0 signals in different p_T bins after like-sign (panels a,c) and track-rotation (panels b,d) subtraction. Taken from [20].

At Fig. 3.3 can be seen preliminary results from p+p collisions $\sqrt{s} = 200$ GeV from 2012. These data are compared with published data from 2009 [20] and FONLL.

3.1.2 Au+Au results

The data sample consisted of Au+Au collisions with $\sqrt{s_{NN}} = 200\ GeV$ from 2010 and 2011, total of 820M of vpd minimum-bias and 240M central events were collected. D^0 production was measured via hadronic decay channels $D^0 \to K^-\pi^+$ and $D^0 \to K^+\pi^-$. Momentum range was $0.0 \leq p_T \leq 6.0\ GeV/c$. D^0 meson invariant mass was reconstructed via same-event

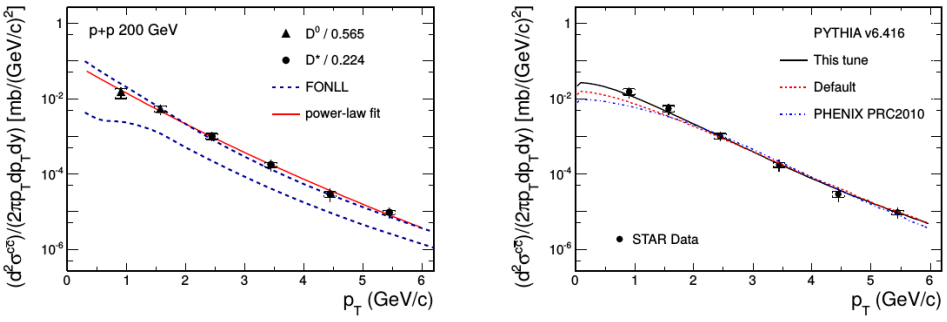

Figure 3.2: Cross section of $c\bar{c}$ with theoretical prediction - FONLL pQCD (left side) and PYTHIA (right side). Taken fron [20].

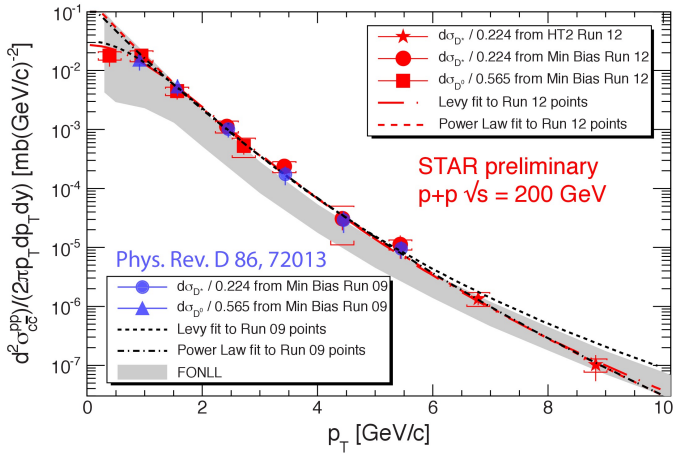

Figure 3.3: Production cross-section of $c\bar{c}$ in p+p collisions at $\sqrt{s} = 200$ GeV from 2012 data. Blue symbols are data from 2009, red symbols are preliminary results from 2012 data. The vertical bars (brackets) represents statistical (systematics) uncertainties. Taken from [21].

method and combinatorial background was reconstructed via mixed-event method. Differential invariant yield of D^0 is shown at 3.4.

Figure 3.5 shows measured R_{AA} of D^0 for semi-central/peripheral (40-80%), central (10-40%) and most central (0-10%) Au+Au collisions. Result from most-central collisions are compared to several theoretical models. For semi-central/peripheral (40-80%) there si no clear evidence for suppression as all data are close to unity within error bars. For central collisions (10-40%) there is some evidence of suppression in region $p_T \geq 3.0\ GeV$. Most central (0-10%) collisions shows clear evidence of suppression, about 0.5 for $p_T \geq 3.0\ GeV/c$. These results are consistent with measurements of electron from heavy flavour hadron decays and light hadrons.

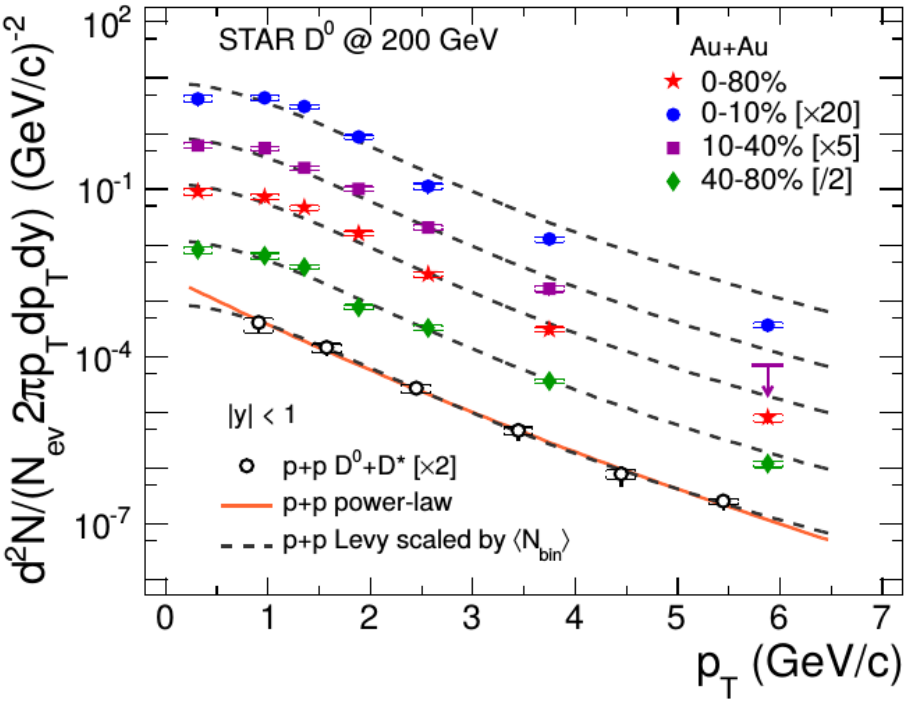

Figure 3.4: Differential invariant yield of D0 with centrality dependence. Solid symbols represents result from Au+Au collisions with different centrality classes, open circles represents p+p results. Taken from [22].

3.2 Results from ALICE

The ALICE detector at LHC as dedicated heavy-ion collision experiment have same goal as STAR: study the QGP. At LHC are collided following systems: p+p, p+Pb, Pb+Pb. Maximum energy for p+p collisions is $\sqrt{s} = 13\ TeV$, for Pb+Pb is $\sqrt{s_{NN}} = 5.02\ TeV$. Measurement of D^0 at p+Pb and Pb+Pb collisions will be discussed. Main sources for this section is [26], [27] and [25].

3.2.1 p+Pb results

The p+Pb collisions serves mainly as control geometry to study the "cold-nuclear matter" (CNM) effects. The CNM effects are not related to formation of QGP and originates from initial and final state. Analysis of CNM effects via results from p+Pb collisions is needed too correct interpretation of heavy-ion collisions.

The D^0 were measured at p+Pb collisions and reconstructed via hadronic decay channel. At 3.6 are show invariant masses of D^0, D^+ and D^{*+}. The R_{pPb} and differential cross section for D^0 meson are shown at 3.7, combined

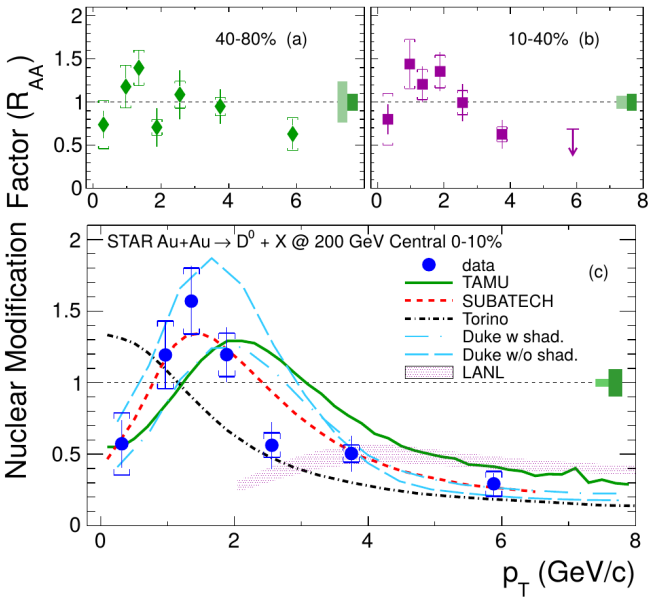

Figure 3.5: R_{AA} of D0 as function of p_T from Au+Au collisions for various centrality classes: 40-80% (a), 10-40% (b) and 0-10% most central collisions (c). Most central data are compared with model calculations: TAMU (solid curve), SUBATECH (dashed curve), Torino (dot-dashed curve), Duke (long-dashed and long-dot-dashed curve) and LANL groups (filled band). Taken from [22].

with data from Pb+Pb collisions. No clear evidence for suppression (or lack of suppression) is shown, as data are more or less equivalent with unity within error bars.

3.2.2 Pb+Pb results

Figure 3.8 shows comparison as function of centrality of the nuclear modification factor of D mesons and of J/ψ from decay of B mesons (J/ψ data are result of CMS collaboration). This result indicated stronger suppression for D mesons (charm quark respectively) than for production of bottom quark in central Pb+Pb collisions. Kinematic region was chosen in order to have similar kinematic range for D mesons as for $J\psi$.

3.3 Results from PHENIX

At Run-12 detector PHENIX also taken data from Cu+Au collisions. Mainly modification of J/ψ have been studied - measured from leptonic decay channel. Results are shown at 3.9. Modification of production of J/ψ at Cu+Au

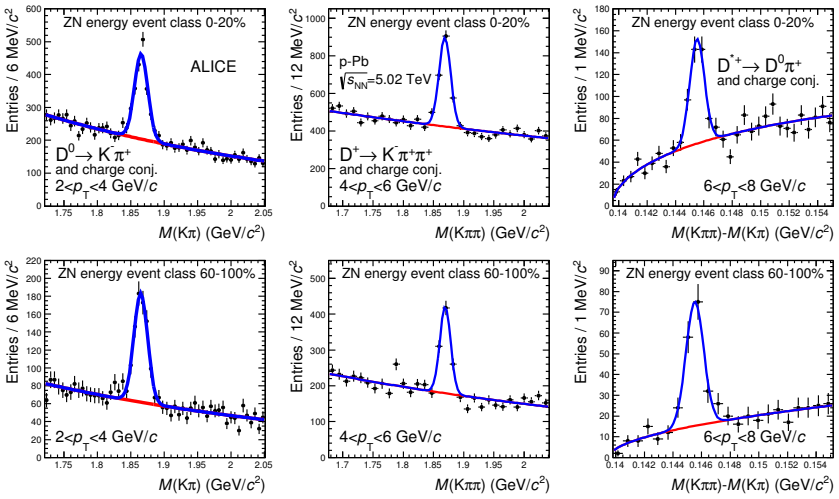

Figure 3.6: Invariant mass of D^0 (left column), $D*$ (center column), and D^{*+} (right column) for two centrality classes from p+Pb collisions. Taken from [25].

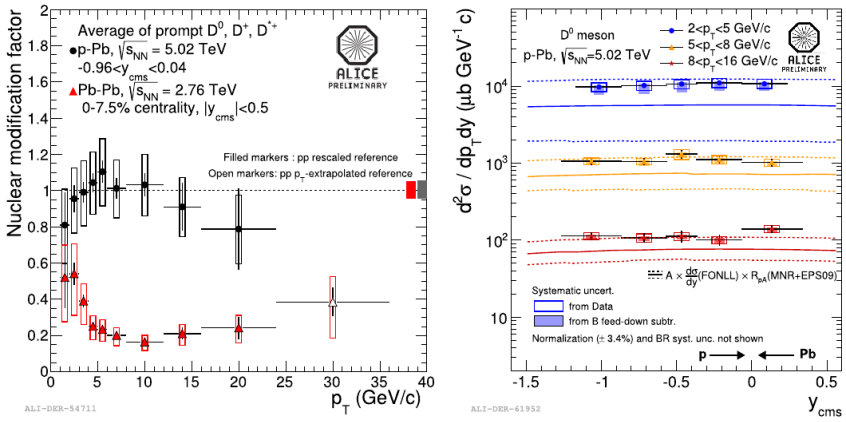

Figure 3.7: Left panel: comparison of average D^0, D^+ and D^{*+} nuclear modification factors R_{pPb} measured in p+Pb collisions and in the 0–7.5% most central Pb+Pb collisions. Right panel: differential cross section for D^0 meson as a function of center-of-mass rapidity y_{CMS}. The continuous and dashed lines represent expectations based on pQCD calculations including EPS09 parametrization of nuclear PDF. Taken from [26].

is more suppressed than at Cu+Cu but less than at Au+Au.

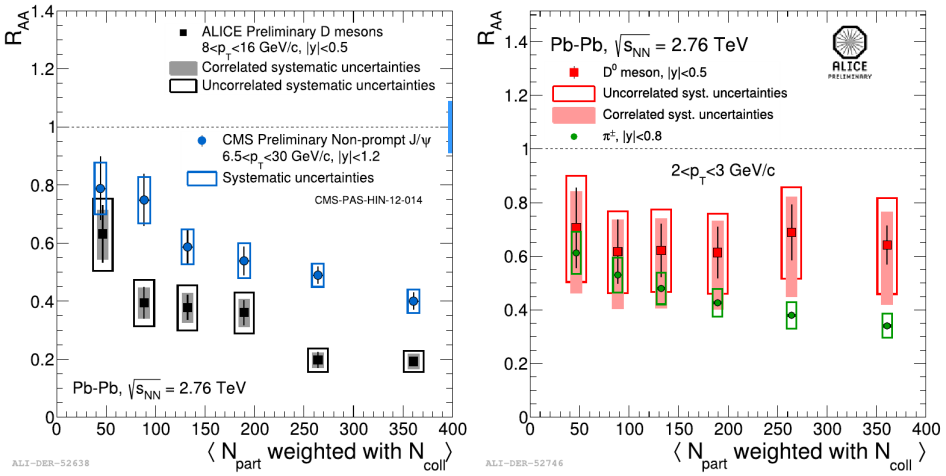

Figure 3.8: Comparison of R_{PbPb} as function of centrality for D mesons and J/ψ. Left panel: Kinematic range $8 < p_T < 16$ GeV for D mesons and $6 < p_T < 30$ GeV for J/ψ from B meson decays. Right panel: R_{PbPb} of D mesons and charged pions in $2 < p_T < 3$ GeV. Taken from [26].

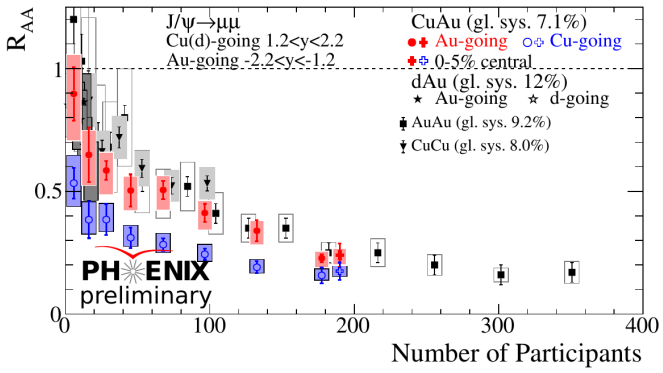

Figure 3.9: Measurement of R_{AuAu} as function of centrality of J/ψ at Cu+Aa collisions with $\sqrt{s_{NN}} = 200\ GeV$, with comparison with Au+Au, Cu+Cu and d+Au results. Taken from [23].

Chapter 4

Analysis of D^0 production in Cu+Au collisions

In this chapter a first results from D^0 meson production analysis will be presented. At first methods of particle identification will be discussed. Next will be disscused selection of analyzed data, event and track selection. Later parts of this chapter are about quality checks and applied corrections.

4.1 Particle identification by TPC and TOF

For particle identification at STAR, the TOF and TPC sub-detectors are used. Due to performance of TOF, it is used for identification in lower p_T (up to 2 GeV/c).

For particle identification by TOF, global tracks are projected to BTOF and geometrically corresponding BTOF channel is linked to it. Result of TOF is velocity of particle β.

Particle identification in TPC is done by particle energy loss per unit length dE/dx. Method of so-called *truncated mean* is used. This method discarded hits with the top 30% of high dE/dx values. Average values from the rest of the tracks are then used for derivation of mean dE/dx of the track. Resolution of TPC for minimum ionizing particle is about 6-8 % for the track with maximum of 45 sampled dE/dx points.

For identification normalized $n\sigma_X^{1/\beta}$ $n\sigma_X^{dE/dx}$ are used. Normalized functions are defined as:

$$n\sigma_X^{1/\beta} = \frac{\frac{1}{\beta^{mea}} - \frac{1}{\beta_X^{th}}}{R^{1/\beta}} \tag{4.1}$$

$$n\sigma_X^{dE/dx} = \frac{ln\frac{< dE/dx >^{mea}}{dE/dx_X^{th}}}{R^{dE/dx}} \tag{4.2}$$

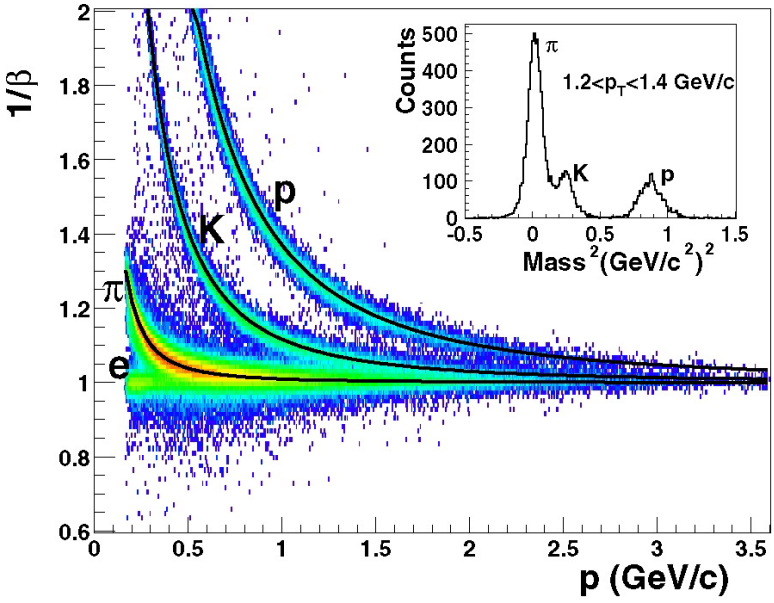

Figure 4.1: Particle identification via TOF. Data from Au+Au collisions. Figure taken from [31]

where X denotes type of particle - in the case of this work, X is a kaon or pion. Superscript *mea* means measured results and the *th* denotes theoretical predictions. The $< dE/dx >$ is mean value of ionization loss in TPC, $R^{1/\beta}$ and $R^{dE/dx}$ are resolutions of TOF or TPC respectively. The $n\sigma^{1/\beta}$ is often reffered as $n\sigma^{TOF}$

4.2 Data selection

Data for this analysis are from Run12 Cu+Au collisions at $\sqrt{s_{NN}} = 200$ GeV. Only about 30% of recorded data were reconstructed at the time of this work. It is expected, that results Cu+au collisions with 0-80% centrality should be similar as results from Au+Au collisions with centrality of 40-50%.

Reconstruction of D^0 meson is done in hadronic decay channel: $D^0 \rightarrow K^-\pi^+$ and $\bar{D^0} \rightarrow K^+\pi^-$. D^0 and $\bar{D^0}$ are analysed together to achieve higher statistics.

Criteria for event selection are listed below:

1. Name of production: P15ie (june 2015)
2. Trigger setup name: cuAu_production_2012
3. |TPC_Vz| < 30 cm

4. | VPD_Vz - TPC_Vz | < 3 cm
5. Used trigger: vpd-zdce-tac-protected (ID: 410008)

Track selection criteria:

1. $| \eta | < 1$
2. $0 < TrackFlag < 1000$
3. number of Fit Points ≥ 20
4. $\frac{number\ of\ TPC\ fit\ points}{number\ of\ possible\ TPC\ fit\ points} \leq 0.52$
5. $p_{T,min} > 0.2$ GeV
6. gDCA < 2.0 cm

4.3 Quality assurance

One of the first steps of new analysis is to check basic quality of selected data. This check of quality includes control of multiplicity by run, reference multiplicity, vertices and more. From this check bad runs are identified and they are not included in analysis itself.

At Fig. 4.2 can be seen reference multiplicity of Cu+Au collisions. These results are consistent with theoretical predictions.

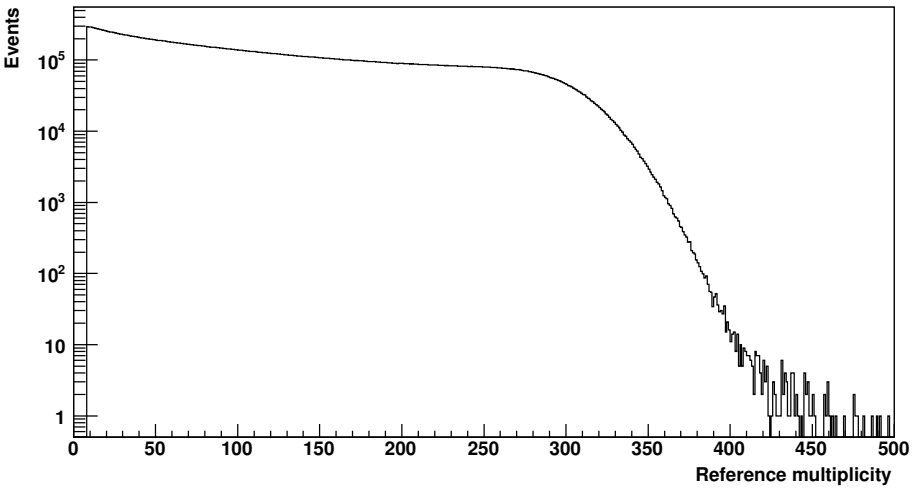

Figure 4.2: Reference multiplicity of Cu+Au collisions at logarithm scale.

Figure 4.3 shows dependence of TOF multiplicity on reference multiplicity after applying cut:

1. Cut 1: TOF multiplicity $<$ 95+5.3$\times$ Reference multiplicity
2. Cut 2: TOF multiplicity $>$ 65+2.8$\times$ Reference multiplicity

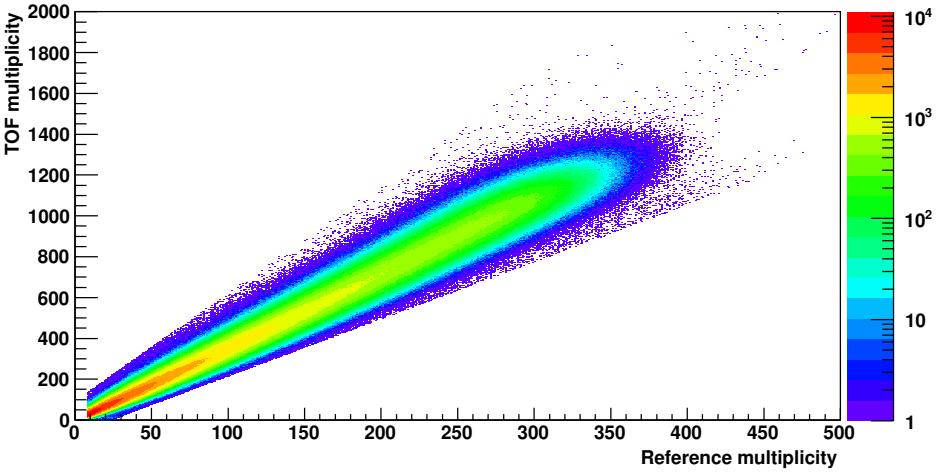

Figure 4.3: TOF multiplicity as function of reference multiplicity.

4.4 Identification of pions and kaons

To obtain D^0 signal pions and kaons must be identified at first. Identification of particles goes as described upper.

Applied cuts for pions identification:

1. $p_T > 0.2$ GeV
2. $|n\sigma_{\pi}^{1/\beta}| < 2$
3. $|n\sigma_{\pi}^{dE/dx}| < 2$

Figures 4.4, 4.5 shows steps in π mesons identification as plots from TOF (4.4) and TPC (4.5).

Applied cuts for identification of kaons:

1. $p_T > 0.2$ GeV/c
2. $|n\sigma_{Kaon}^{1/\beta}| < 2$
3. $|n\sigma_{Kaon}^{dE/dx}| < 2$

As in the case of identification of π mesons, identification of kaons are show at three figures: Fig. 4.6 shows obtained signal from TOF, Fig. 4.7 shows signal from TPC.

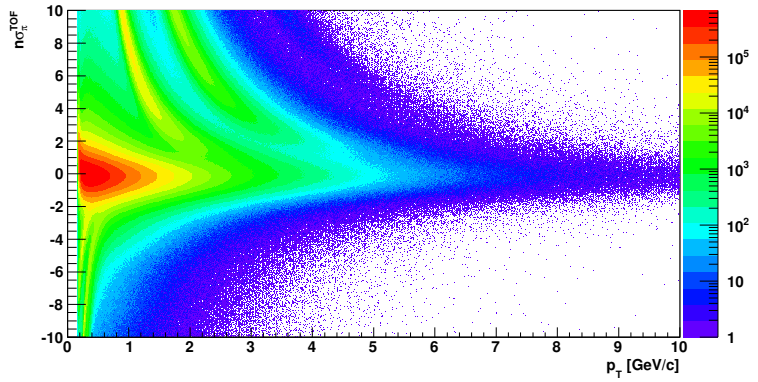

Figure 4.4: Particle identification of π mesons via TOF. The $n\sigma_{1/\beta}$ as function of p_T.

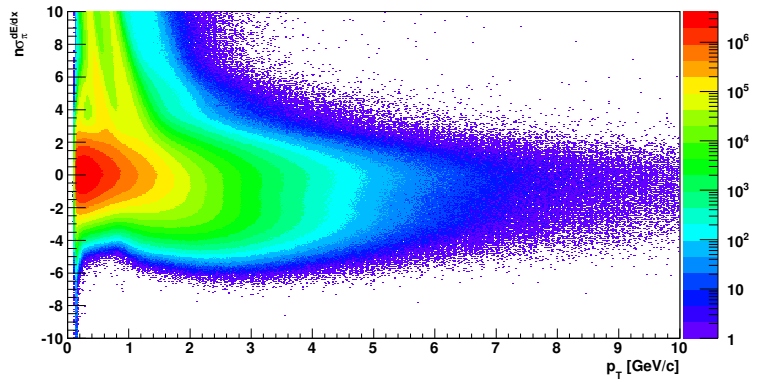

Figure 4.5: Particle identification of π mesons via TPC. The $n\sigma_{dE/dx}$ as function of p_T.

4.5 Raw D^0 yield

With identified π mesons and kaons, the $K^-\pi^+$ and $K^+\pi^-$ can be combined to obtain invariant mass. But kaon and π pairs can be from $D^0, \bar{D}^0$ decays, from another decays and combinatorial background. Primarily *mixed event*, $like-sign$ and *rotated momentum* method is used for reconstruction of combinatorial background.

Mixed event method paired a unlike-sign $K\pi$ pairs from different events. To keep similar characteristic of mixed events, the data sample was divided into 10 bins in multiplicity and 10 bins in collisions vertex along the beam. Only pairs from events with same characteristics were mixed. Mixed event method is the main method for reconstruction of combinatorial background of this analysis.

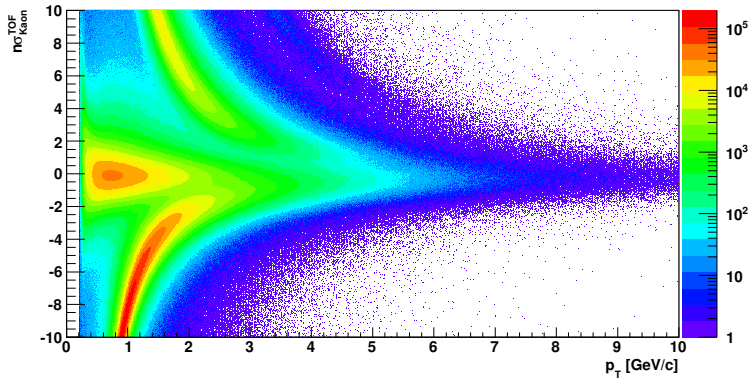

Figure 4.6: Particle identification of kaons via TOF. The $n\sigma_{1/\beta}$ as function of p_T.

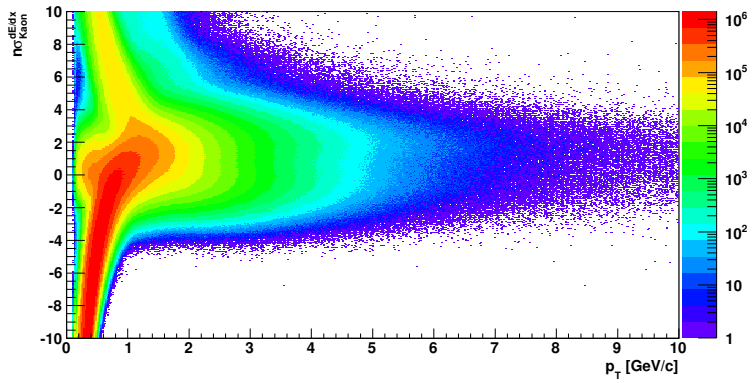

Figure 4.7: Particle identification of kaons via TPC. The $n\sigma_{dE/dx}$ as function of p_T.

Like-sign method paired pions with the kaons of the same charge. It is widely used method and is believed, that the pair combination produce background without any correlations.

Rotated momentum method paired each pion candidate with the kaon candidate with reversed 3-momentum. Track rotation technique is based on the assumption that by rotating one of the daughter track for 180 degree the kinematics of decay is destroyed and thus the distribution of a pair invariant mass with one track rotated is able to reproduce te random combinatorial background.

Fig. 4.8 shows raw yield of D^0 mesons obtained by mixed event method and Fig. 4.9 show raw yield obtained by like sign method and Fig. 4.10 shows raw yield of D^0 mesons obtained by rotated momentum method. After subtraction of combinatorial background, signal was fitted by Gaussian and

background by linear function. Overview of raw yield by various method can be seen at 4.1. Mean of Gaussian within errors from all method is comparable with the PDG value 1.86483 $\pm$ 0.00014 GeV/c^2. Signal from D^0 mesons can be seen at all figures.

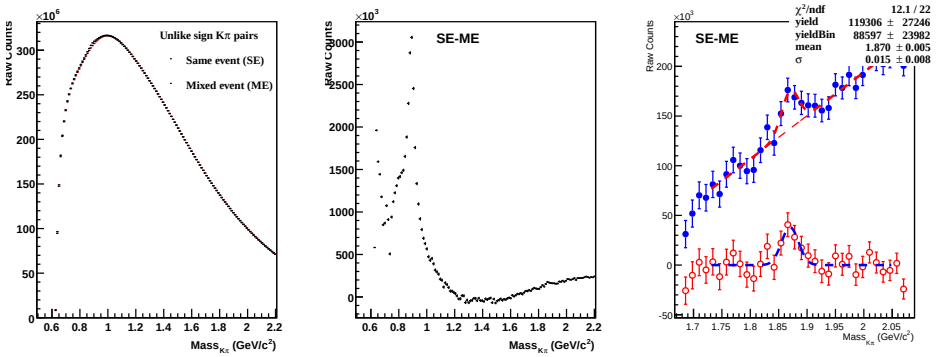

Figure 4.8: Raw Yield of D^0 meson - Mixed event method. Left panel: Invariant mass distribution of $K\pi$ pairs. Same event is displayed by black dost, Mixed events by red dots. Central panel: Distribution of $K\pi$ pairs invariant mass after after subtraction of mixed events from same events. Right panel: Invariant mass in region of D^0 mesons. Background is fitted by linear function, signal is fitted by Gaussian. Blue points represents signal with residual background, red open points represents signal after subtraction of residual background.

Method	Raw yield	Mean [GeV/c^2]
Mixed event	119306 $\pm$ 27246	1.870 $\pm$ 0.005
Like-sign	92747 $\pm$ 34308	1.874 $\pm$ 0.007
Rotated momentum	99443 $\pm$ 35235	1.866 $\pm$ 0.006

Table 4.1: Overview of D^0 meson raw yield by mixed event mehod, like-sign method and rotated momentum method. Mean is a mean of Gaussian

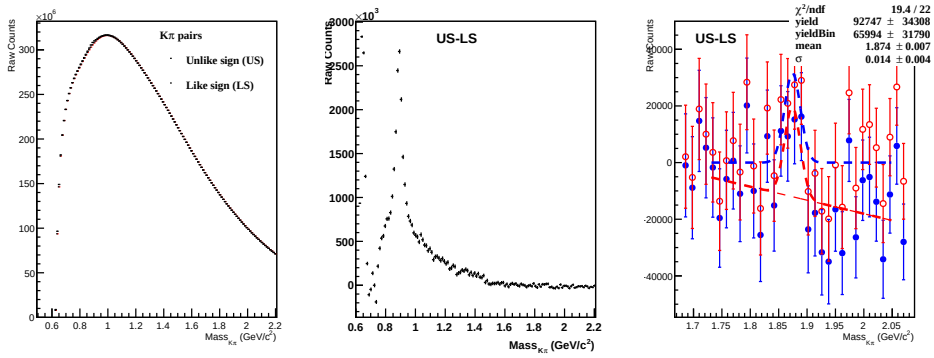

Figure 4.9: Raw Yield of D^0 meson - LS method. Left panel: Invariant mass distribution of $K\pi$ pairs. Unlike sign event is displayed by black dost, like sign events by red dots. Central panel: Distribution of $K\pi$ pairs invariant mass after after subtraction of like sign events from unlike sign events. Right panel: Invariant mass in region of D^0 mesons. Background is fitted by linear function, signal is fitted by Gaussian. Blue points represents signal with residual background, red open points represents signal after subtraction of residual background.

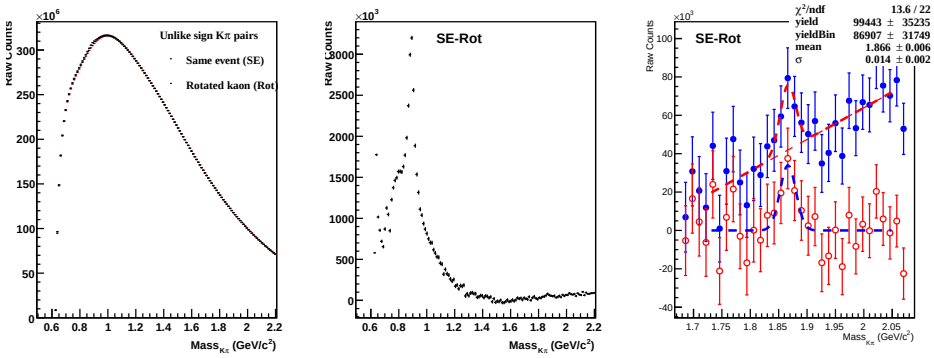

Figure 4.10: Raw Yield of D^0 meson - ROT method. Left panel: Invariant mass distribution of $K\pi$ pairs. Same event is displayed by black dost, rotated kaons by red dots. Central panel: Distribution of $K\pi$ pairs invariant mass after after subtraction of rotated kaons from same events. Right panel: Invariant mass in region of D^0 mesons. Background is fitted by linear function, signal is fitted by Gaussian. Blue points represents signal with residual background, red open points represents signal after subtraction of residual background.

Conclusion

Goals of this work are two: at first author of this thesis should become acquainted with STAR detector and with the physics of ultra-relativistic heavy-ion collisions. This is done in chapter 1, 2 and 3. At the first chapter RHIC and STAR detector are presented with description of sub-detectors of STAR which are used in this analysis. Moreover overview of current and planned runs are present. First chapter are closed by illustration of RHIC future - sPHENIX detector and upgrade of RHIC - eRHIC. Chapter 2 consist of theoretical overview, from Standard model of particle physics to theory of strong interaction - QCD. Heavy-ion collisions and D^0 mesons are described too. First goal of this work are finished at chapter 3 where overview of experimental results about D^0 mesons are shown.

Second goal of this work is analysis of D^0 meson production in Cu+Au collisions. Author of this work become acquainted with analysis code and done basic quality assurance. Results of this work can be seen at chapter 4. Identification of kaons and pions is shown with raw yield of D^0 mesons achieved via various methods for reconstructing combinatorial background. Signal can be seen and thus analysis should continue.

Next steps in the analysis are to include correction on the detector effects, corrections on multiplicity and evaluated systematic errors and obtain corrected yield of D^0, invariant yield of D^0 and Nuclear modification factor of D^0.

Bibliography

[1] STAR Images [online]. STAR Collaboration. [cit. 2016-04-03]. https://drupal.star.bnl.gov/STAR/public/img

[2] OZAKI, S. a T. ROSER. Relativistic Heavy Ion Collider, its construction and upgrade. Progress of Theoretical and Experimental Physics [online]. 2015, 2015(3), 3A102-0 [cit. 2016-04-03]. DOI: 10.1093/ptep/ptu093. ISSN 2050-3911. http://ptep.oxfordjournals.org/cgi/doi/10.1093/ptep/ptu093

[3] RUN OVERVIEW OF THE RELATIVISTIC HEAVY ION COLLIDER [online]. [cit. 2016-04-04]. http://www.rhichome.bnl.gov/RHIC/Runs/index.htm

[4] ANDERSON, M., J. BERKOVITZ, W. BETTS, et al. The STAR time projection chamber: a unique tool for studying high multiplicity events at RHIC. Nuclear Instruments and Methods in Physics Research Section A: Accelerators, Spectrometers, Detectors and Associated Equipment [online]. 2003, 499(2-3), 659-678 [cit. 2016-04-05]. DOI: 10.1016/S0168-9002(02)01964-2. ISSN 01689002. http://linkinghub.elsevier.com/retrieve/pii/S0168900202019642

[5] An Upgrade Proposal from the PHENIX Collaboration, arXiv:1501.06197. [online]. [cit.2016-04-04].

[6] E.C. Aschenauer, et al., eRHIC Design Study: An Electron-Ion Collider at BNL , arXiv:1409.1633 (2014).

[7] SARKAR, S, H SATZ a B SINHA. The physics of the Quark-Gluon plasma: introductory lectures. New York: Springer, c2010, ix, 369 p. Lecture notes in physics, 785. ISBN 3540769676

[8] RAK, Jan a Michael J TANNENBAUM. High-pT physics in the heavy ion era. x, 387 p. ISBN 0521190290.

[9] Tlustý D. A Study of Open Charm Production in p+p Collisions at STAR, Ph.D. thesis, Prague 2014

[10] Vajzer M. Study of hard processes in the ALICE experiment, Ph.D thesis, Prague 2015

[11] GYULASSY, Miklos. The QGP Discovered at RHIC. [online]. [cit. 2016-03-10]. http://arxiv.org/abs/nucl-th/0403032

[12] Why is the Higgs discovery so significant? STFC [online]. [cit. 2016-04-07]. https://www.stfc.ac.uk/2861.aspx

[13] K. Yagi et al., Quark-gluon plasma, Cambridge University Press, (2005)

[14] RAK, Jan a Michael J TANNENBAUM. High-pT physics in the heavy ion era. x, 387 p. ISBN 0521190290.

[15] MCNULTY WALSH, Karen. Supercomputing the Transition from Ordinary to Extraordinary Forms of Matter: Calculations plus experimental data help map nuclear phase diagram, offering insight into transition that mimics formation of visible matter in universe today. BROOKHAVEN NATIONAL LABORATORY. Http://www.bnl.gov [online]. 2013 [cit. 2016-03-12]. http://www.bnl.gov/newsroom/news.php?a=24281

[16] K.A. Olive et al. (Particle Data Group), Chin. Phys. C, 38, 090001 (2014) and 2015 update.

[17] LHCb COLLABORATION. Observation of the resonant character of the Z(4430)$^-$ state. In: [online]. 2014 [cit. 2016-03-23]. http://arxiv.org/abs/1404.1903

[18] CHÝLA, Jiří. Quarks, Partons and Quantum Chromodynamics. Skriptum MFF UK 2009. Available from: http://www-hep2.fzu.cz/ chyla

[19] Adare A., C. Aidala, et al. Measurements of directed, elliptic, and triangular flow in Cu+Au collisions at $\sqrt{s_{NN}} = 200$ GeV. [cit. 2016-02-05] http://arxiv.org/abs/1509.07784v1

[20] ADAMCZYK, L., G. AGAKISHIEV, M. M. AGGARWAL, et al. Measurements of D 0 and D * production in p + p collisions at s = 200 ? ? GeV. Physical Review D [online]. 2012, 86(7), - [cit. 2016-06-03]. DOI: 10.1103/PhysRevD.86.072013. ISSN 1550-7998. http://link.aps.org/doi/10.1103/PhysRevD.86.072013

[21] ZHENYU Ye for STAR Collaboration, Open Charm Hadron Production in p+p, Au+Au and U+U Collisions at STAR. Nuclear Physics A 00 (2014) 1–4

[22] ADAMCZYK, L., J.?K. ADKINS, G. AGAKISHIEV, et al. Observation of D 0 Meson Nuclear Modifications in Au + Au Collisions at $\sqrt{s_{NN}} =$

200 GeV. Physical Review Letters [online]. 2014, 113(14), - [cit. 2016-06-03]. DOI: 10.1103/PhysRevLett.113.142301. ISSN 0031-9007. Dostupné z: http://link.aps.org/doi/10.1103/PhysRevLett.113.142301

[23] Forward/backward J/ψ production in Cu+Au collisions at PHENIX. Journal of Physics: Conference Series [online]. [cit. 2016-06-03]. ISSN 1742-6588.

[24] ADAM, J., D. ADAMOVÁ, M. M. AGGARWAL, et al. Measurement of charm and beauty production at central rapidity versus charged-particle multiplicity in proton-proton collisions at $sqrts$ = 7 TeV. Journal of High Energy Physics [online]. 2015, 2015(9), - [cit. 2016-06-03]. DOI: 10.1007/JHEP09(2015)148. ISSN 1029-8479. http://link.springer.com/10.1007/JHEP09(2015)148

[25] ALICE Collaboration. Measurement of D-meson production versus multiplicity in p-Pb collisions at 5.02 TeV. [cit. 2016-04-20] arXiv:1602.07240

[26] Measurement of D-meson production in pp, p-Pb and Pb-Pb collisions with ALICE at the LHC, ALICE Collaboration (2014) Nuclear Physics A, 932 , pp. 51-56.

[27] ADAM, J., D. ADAMOVÁ, M. M. AGGARWAL, et al. Centrality dependence of high-pT D meson suppression in Pb-Pb collisions at $sqrts_{NN}$ = 2.76 TeV. Journal of High Energy Physics [online]. 2015, 2015(11), - [cit. 2016-06-03]. DOI: 10.1007/JHEP11(2015)205. ISSN 1029-8479. Dostupné z: http://link.springer.com/10.1007/JHEP11(2015)205

[28] Beam Use Request, STAR Collaboration. [cit. 7.5.2016] https://drupal.star.bnl.gov/STAR/starnotes/public/sn0657

[29] AAIJ, R., B. ADEVA, M. ADINOLFI, et al. Observation of J/ψ Resonances Consistent with Pentaquark States in $\Lambda_b^0 \to J/\psi K^- p$ Decays. Physical Review Letters [online]. 2015, 115(7), [cit. 2016-06-21]. DOI: 10.1103/PhysRevLett.115.072001. ISSN 0031-9007. http://link.aps.org/doi/10.1103/PhysRevLett.115.072001

[30] Why is the Higgs discovery so significant? STFC [online]. [cit. 2015-06-07]. https://www.stfc.ac.uk/2861.aspx

[31] STAR Collaboration, Pion, kaon, proton and anti-proton transverse momentum distributions from p+p and d+Au collisions at 200 GeV, Phys. Lett. B 616, 2005